Horizontally and Vertically Aligned Polymeric Nanosheets: CO₂-Induced Morphological Changes of Block Copolymer Thin Films

Hideaki Yokoyama,*,† Lei Li,‡ Cedric Dutriez,‡ Yuko Iwakura,‡ Kenji Sugiyama,§ Hiroyasu Masunaga,§ Sono Sasaki,§ and Hiroshi Okuda#

Graduate School of Frontier Sciences, The University of Tokyo, 5-1-5 Kashiwa-no-ha, Kashiwa, Chiba 277-8561, Japan, Nanotechnology Research Institute, National Institute of Advanced Industrial Science and Technology, Central 5, Higashi, 1-1-1, Tsukuba, Ibaraki 305-8565, Japan, Department of Organic and Polymeric Materials, Tokyo Institute of Technology, 2-12-1, Ohokayama, Meguro-ku, Tokyo 152-8552, Japan, Japan Synchrotron Radiation Research Institute, 1-1-1, Kouto, Sayo-cho, Sayo-gun, Hyogo 679-5198, Japan, and International Innovation Center, Kyoto University, Sakyo-ku, Kyoto 606-8501, Japan

Received July 4, 2008; Revised Manuscript Received September 19, 2008

ABSTRACT: Recently, the carbon dioxide (CO_2) process with sphere forming block copolymer (bcp) templates successfully introduced nanometer cells into polymeric materials. CO_2 selectively swells CO_2-philic domains of fluorinated blocks and introduces nanometer voids in the CO_2-philic domains. We extended the same methodology to bcp templates with nonspherical domains. Depending on the initial morphologies controlled by selectivity of casting solvents, vertically or horizontally aligned polymer nanosheets spontaneously appeared after the CO_2 process and were confirmed by scanning electron microscopy and grazing incident small-angle X-ray scattering. Selective swelling of minority domains with CO_2 induces transition to lamellar morphology during the process and results in stacking sheet structure after depressurization of CO_2.

Introduction

Block copolymer (bcp) templates have been intensively studied to fabricate a variety of nanostructures.[1,2] Creating nanocellular and porous polymeric materials using bcp templates is a branch of objectives of the bcp template techniques. A well-documented methodologies[3] to fabricate porous polymeric materials are based on decomposition of particular bcp domains using ozone,[4] biodegradation,[5] and ultraviolet (UV) light.[6] In such decomposing methods, pore shape and size are identical to those of the decomposed domains and, therefore, size, shape, and order of pores can be precisely predicted. In other words, the available structures are limited to the equilibrium bcp morphologies. We have reported the alternative approach that CO_2 as a porogen is introduced into particular bcp domains to create nanometer cells.[7,8] The CO_2-philic semifluorinated block domains of bcps work as nuclei of CO_2 bubbles and introduce nanometer cells. The size of cells can be tuned by changing process conditions with the same template. Moreover, this methodology can be applied to thin films[9,10] as well as monoliths and also to another sphere forming nonfluorine bcp, a block copolymer of polystyrene, and CO_2-philic polydimethylsiloxane.[11]

Here we report that selective swelling with CO_2 of bcp thin films induces morphological changes and results in unique nanosheet structures that differ from the original bcp morphology. Horizontally or vertically stacked nanosheet structures of bcp bilayers on substrates appeared as a result of the CO_2 process. The orientation of the nanosheets can be controlled by initial as-cast morphologies, which can be altered by the selectivity of casting solvents.

Experimental Section

Materials. We synthesized two batches of polystyrene-*b*-poly-(perfluorooctylethyl methacrylate) (PS-PFMA) by sequential living anionic polymerization. The detail of the synthesis is found elsewhere.[12] The molecular weights of PS-PFMAs are 20000−13000 and 10000−7670 g mol⁻¹. We prepared a mixture of the PS-PFMAs to adjust the volume fraction of PFMA to 33 vol %. The molecular weights of the PS blocks were determined by gel permeation chromatography, and the molecular weights of the PFMA blocks were determined by ¹H NMR.

α,α,α-Trifluorotoluene (Aldrich) and hexafluorobenzene (Aldrich) were used as spin-casting solvents and were named as TFT and HFB, respectively. TFT and HFB are a neutral solvent and selective solvent for PFMA, respectively. PS-PFMA films (500 nm thick) were prepared by spin-casting of those solutions onto silicon wafers. The silicon wafers (Shinetsu Co.) were used as received.

Carbon Dioxide Process. A custom-designed stainless steel high-pressure vessel for the CO_2 process was connected to a high-pressure liquid chromatography pump (JASCO PU-2086 plus) equipped with a cooling head, and to a programmable backpressure regulator (JASCO SCF-Bpg). Si wafers coated with the copolymer thin films were placed in the high-pressure vessel and pressurized with CO_2 at 60 °C for 1 h with a constant pressure controlled by the backpressure regulator. The vessel was placed in an ice bath to quench the temperature to 0 °C, while maintaining the pressure constant by continuous pumping and back-pressure control. Depressurization rate was 0.5 MPa/min for all the processes.

Characterization. To expose internal structures to the surfaces, a reactive ion etcher (RIE, SAMCO Compact Etcher FA-1) was used with a CF₄ flow rate of 2 mL/min, pressure of 10 Pa, and power density of 10 W/cm². Under this condition, the etching rate for PS-PFMA copolymer thin films was approximately 1 nm/s. After 30-nm etching by RIE, the surface topography was characterized by atomic force microscope (AFM, Seiko SPA 300HV). AFM measurements were performed in the tapping mode, and both topographic and phase images were obtained simultaneously. We used silicon tips with a spring constant of 22 N/m. RIE removes the homogeneous surface-covering layer and introduces topographic

* To whom correspondence should be addressed. E-mail: yokoyama@molle.k.u-tokyo.ac.jp. Tel./Fax: +81-4-7136-3766.
† The University of Tokyo.
‡ National Institute of Advanced Industrial Science and Technology.
§ Tokyo Institute of Technology.
# Japan Synchrotron Radiation Research Institute.

contrast due to slightly different etching rates of PS (slow) and PFMA (fast) domains embedded in the films.

The specimens for cross-sectional transmission electron microscopy (TEM) were prepared as follows: An as-cast thin film was peeled off from the silicon wafer onto the surface of water. The floated film was picked up onto a cured epoxy plate and then embedded into the same epoxy. The specimens were stained using ruthenium tetroxide. Cryo-microtoming was used to obtain cross-sectional slices from the epoxy monolith for TEM observations.

The films after the CO_2 process were scratched in liquid nitrogen for cross-sectional views. Structures on the cryo-fractured surfaces were observed using an environmental scanning electron microscope (ESEM; Philips XL20 ESEM-FEG) equipped with a field emission gun. To avoid a possible artifact, no conductive coating was employed. Five to 6 keV of electron beam was used for the observation with working distance of less 10 mm.

Grazing incident small-angle X-ray scattering (GISAXS) experiments were conducted at BL-40B2 beamline of SPring-8 synchrotron facility and at 15A beamline of Photon Factory in KEK. A sample was placed in a vacuum chamber with Kapton windows on a computer controlled gonio stage. The X-ray beam impinges at a small incident angle α onto a thin film supported on a substrate. The scattered X-ray was detected with an image intensifier accompanied with a two-dimensional charge coupled device camera. Experimental detail of GISAXS at SPring-8 can be found elsewhere.[13] The wave vectors are defined as $q_y = (2\pi/\lambda) \sin \theta \cos \beta$ and $q_z = (2\pi/\lambda)(\sin \alpha + \sin \beta)$, where θ is the inplane angle, α and β are incident and scattered vertical angles to the surface plane, respectively, and λ is a wavelength (1.5 Å).

Results and Discussion

Morphologies of As-Cast Films. Fluorinated polymers are immiscible with most of ordinary polymers. Interaction parameters between a typical fluorinated polymer and polystyrene varies from 0.4 to unity.[14] Therefore, for block copolymers with fluorinated blocks, the degree of segregation (χN), which is scaled by the product of interaction parameter (χ) and the number of monomer (N), easily reaches strong segregation regime. Due to such strong repulsive interaction between PS and fluorinated blocks, diffusion of block copolymers with fluorinated blocks in ordered domain structures is practically hindered,[15] and the morphology is easily trapped in nonequilibrium one. In addition, when the specimens are prepared by casting block copolymer solutions, the morphologies are strongly influenced by the choice of casting solvents.[16] In Figure 1, two different morphologies of the PS-PFMA films spun-cast from two different solvents are displayed. The panels a and b are atomic force microscope (AFM) topographical images after reactive ion etching (RIE), which etches away a 30 nm thick layer from the surface. Without etching, we did not find significant topographical patterns on the surface. Because fluorinated polymers have the lower surface energies than that of PS, the surfaces of those copolymers are totally covered with the PFMA domains.[17] RIE removes the homogeneous surface covering PFMA layer and introduces topographical contrast due to slightly different etching rate of PS (slow) and PFMA (fast) domains embedded in the films.[9,10] The PS-PFMA film prepared from TFT, a neutral solvent, shows in Figure 1a network-like domains of PFMA (dark) with many defects without specific symmetry. On the other hand, when HFB, a selective solvent for shorter CO_2-philic PFMA blocks, is chosen, we observed completely different morphology as shown in Figure 1b. The AFM contrast originates from the faster etching rate of PFMA than that of PS, and thus, the PFMA domain is lower (darker) than the PS domains. Therefore, Figure 1b indicates that thin walls of the PFMA domains separate relatively large circular PS domains. It can be speculated that spherical micelles are accumulated on the substrate because the PS is insoluble in HFB and the block copolymer is expected to form inverse micelles
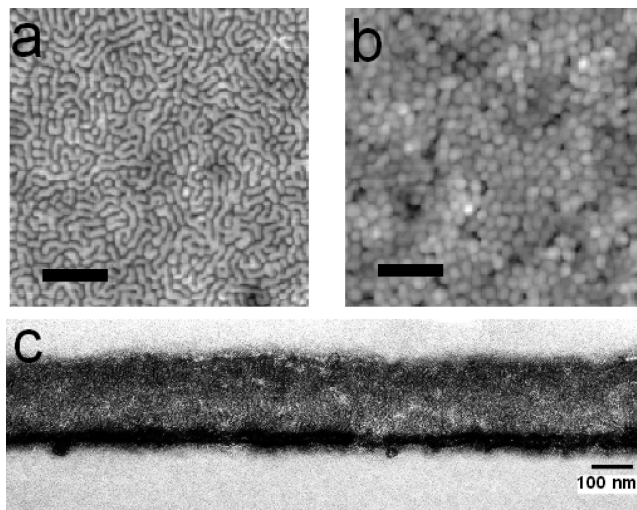

Figure 1. As-cast morphologies of the films spun-cast from (a) TFT and (b) HFB revealed by AFM after reactive ion etching, and the cross-sectional TEM image (c) of the film spun-cast from HFB solution and stained with ruthenium tetroxide. The bars in (a) and (b) indicate 200 nm.

with large PS cores with short PFMA coronas in HFB. However, the cross-sectional transmission electron microscope image in Figure 1c suggests that the PS domains show some connectivity in the film thickness direction.[18]

To support the AFM and TEM observations, we performed GISAXS analysis of the as-cast films. The as-cast films were exposed to grazing incident X-ray as described in Experimental Section. The GISAXS patterns of 500-nm-thick films spun-cast from TFT and HFB solutions are shown in Figure 2a and b respectively. In case of the film spun-cast from TFT, a semicircular pattern of Bragg peak is observed. The lower half of the circular pattern is hindered by the total reflection of the substrate at 0.15 degree of incident X-ray, which is just slightly above the critical angle of the polymer thin film but well below the critical angle of the substrate (silicon). The wing-like pattern at $q_z = 0.25$ along q_y axis is called the Yoneda wing, which is located at the critical angle of the material under investigation. The direct and specularly reflected X-rays were blocked with a rectangular beam stopper (q_z: 0−0.3 nm^{-1}) and rectangular attenuator (q_z: 0.3−0.6 nm^{-1}). The semicircular pattern above the Yoneda wing clearly indicates that there is no directional anisotropy in the morphology in the cross-sectional plane of the film. This conclusion from GISAXS is consistent with the AFM image in Figure 1a. On the other hand, the films spun-cast from HFB shows the scattering maxima in the proximity of the Yoneda wing as shown in Figure 2b, which indicates that the morphology of the film spun-cast from HFB is weakly oriented along the z-axis. This result is consistent with the AFM and TEM images in Figure 1b,c and concludes that PS cylinders separated by thin walls of PFMA are weakly oriented to the direction perpendicular to the film. The appearance of vertically oriented PS cylinders can be understood as follows: Large PS cores are surrounded by short PFMA coronas in the HFB solution (inverse micelles). During the spin-casting process, the film shrinks in the thickness direction as the solvent evaporates and the micelles in the swollen film are compressed in the film thickness direction. Therefore, inverse micelles tend to be combined in the film thickness direction and form fat cylinders perpendicular to the film surface.

Intensities as a function of q_y at q_z of the maximum intensities are extracted from Figure 2 and plotted in Figure 3. First-order peaks are clearly found in the films spun-cast both from TFT and HFB. However, the characteristic distance ($2\pi/q_{y,max}$) of
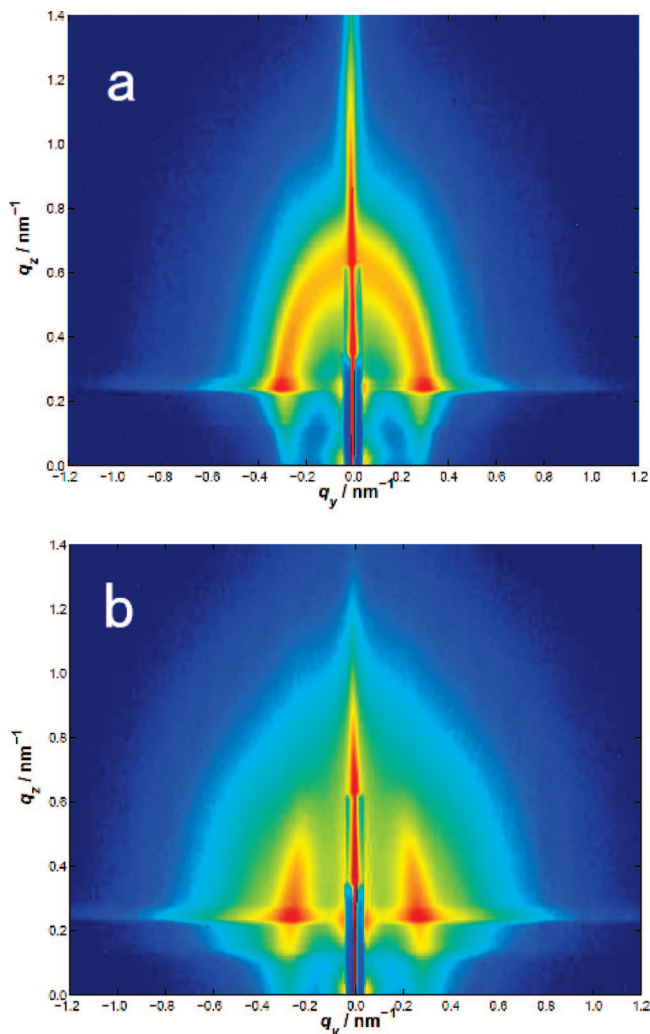
Figure 2. GISAXS patterns of the films spun-cast from (a) TFT and (b) HFB solutions. q_y and q_z are the wave vectors parallel and perpendicular to the film plane, respectively. On the z-axis, a rectangular beam-stopper and attenuator are installed. The incident angle was 0.15 degree.
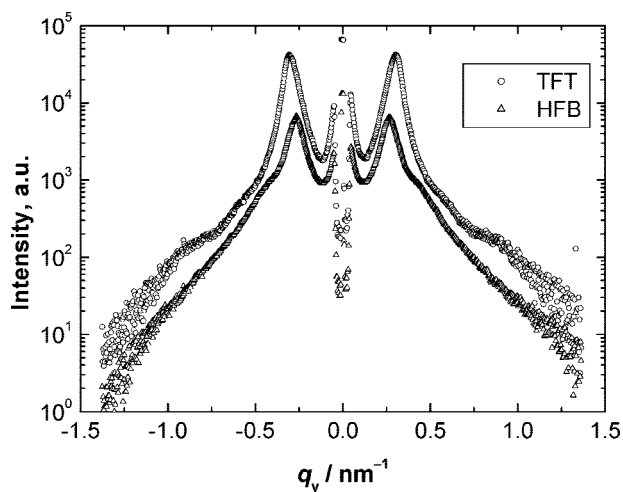

Figure 3. Intensities versus q_y at q_z of the maximum intensities, which are on the Yoneda wings in Figure 2a,b.

HFB (23.4 nm) determined from q_y of the maximum intensity ($q_{y,max}$) is greater than that of TFT (20.7 nm) despite the use of the same polymer. No higher order diffractions are found both in the films spun-cast from TFT and HFB as expected from the
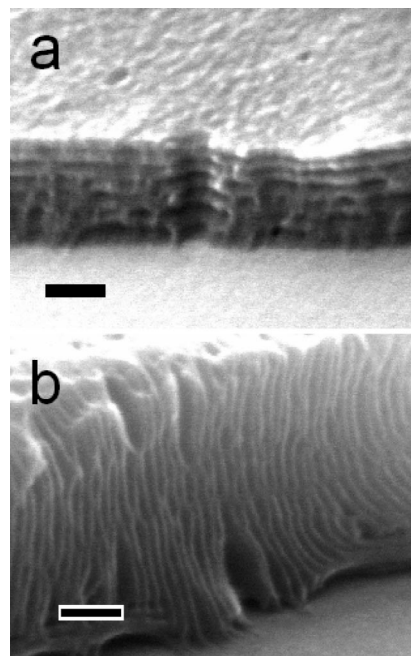

Figure 4. SEM images of nanosheet structures appeared after the CO_2 process. Depending on the initial morphology, the films of the same bcp show different nanosheet structures. Cross-sectional views of nanosheet thin films cast from (a) TFT and (b) HFB after the CO_2 process at a saturation pressure of 8 MPa, followed by scratching at liquid nitrogen temperature. The bars indicate 100 nm.

poorly ordered morphologies in Figure 1. The film spun-cast from TFT clearly shows the shoulders of the form factor in the q-range of $0.5-0.6$ nm^{-1} significantly higher than the q-range of $0.4-0.5$ nm^{-1} of the films spun-cast from HFB. Therefore, the size of the dispersed PFMA domains spun-cast from TFT is smaller than that of the dispersed PS domains in HFB, which is consistent with the AFM images in Figure 1.

Structures after CO_2 Processes. The films with two different initial morphologies were pressurized with CO_2 at 8 MPa and 60 °C for 30 min. The detail of the experimental setting has been described in our previous reports.[7-11] Then the films were thermally quenched to 0 °C, while maintaining the pressure by continuous pumping with backpressure control. This thermal quenching ensures that the CO_2-swollen structures are fixed by the glass transition of PS swollen with CO_2, which occurs approximately at 30 °C,[19,20] which is well below the glass transition temperature (T_g) of PS in air. To confirm that the T_g of PS is the determining factor, we measured the glass transition temperatures (T_gs) of PS-PFMA using differential scanning calorimetry (DSC). The detail of the DSC experiment is in the Supporting Information. The T_g of PFMA was found to be 73 °C, which is lower than that of PS (100 °C) and should be much lower than that of PS in the presence of CO_2 because PFMA is more CO_2-philic and highly plasticized. In addition, PS is the major component of the PS-PFMAs used in this study. Therefore, the determining factor of the process is not the T_g of PFMA, but T_g of PS in CO_2. After the structure was frozen by the glass transition of PS, CO_2 pressure was released at a rate of 0.5 MPa/min. A more detailed analysis of the effect of depressurization temperature relative to the glass transition temperature of CO_2-swollen skeleton domains for fabrication of nanocellular and porous structures will be reported in a separate paper. The films were removed from the high-pressure vessel and the surfaces of the films were scratched with a razor blade at liquid nitrogen temperature to be observed by cross-sectional SEM. The cross-sectional SEM images of the films after the CO_2 process are shown in Figure 4. The film spun-
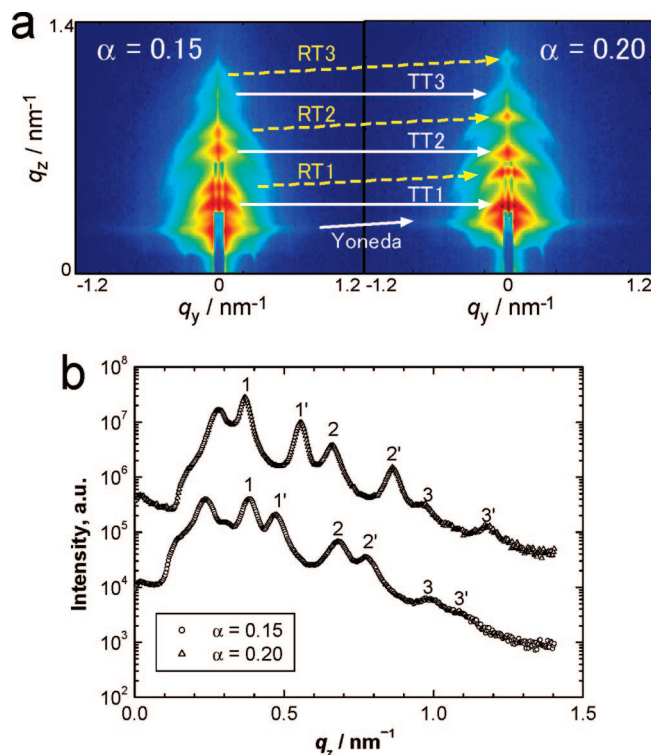
Figure 5. (a) Grazing incident small-angle X-ray scattering (GISAXS) patterns of the nanosheet films. q_y and q_z are the wave vectors parallel and perpendicular to the film plane, respectively. On the z-axis, a rectangular beam-stopper and attenuator are installed. T and R represent transmission and reflection components, respectively. For example, RT2 indicates the second order peak of reflected, scattered, and transmitted X-ray. The GISAXS patterns at two different incident angles α of 0.15 (left) and 0.20 (right) degrees respective to the film plane of nanosheet thin films spun-cast from TFT show peaks on the q_z axis, which indicate layered structures. (b) The intensity versus q_z was plotted. The peaks were assigned to two sets of peaks: 1, 2, and 3 and 1′, 2′, and 3′. 1, 2, and 3 correspond to the first, second, and third order diffraction from layered structure by TT event. On the other hand, 1′, 2′, and 3′ correspond to the first, second, and third order diffraction from layered structure by RT event.

cast from TFT, which shows network-like domains without any preferential orientation before the process, was converted by the CO_2 process to the parallel nanosheets stacking on the substrates, as shown in Figure 4a.

The GISAXS patterns of the same film in Figure 5a show irregularly spaced peaks along the q_z-axis, which are the evidence of the structure developing parallel to the surface. However, the peak positions cannot be assigned to the simple rule for one-dimensionally periodic structures, in which the higher order peaks are integer multiples of the first order peak position. To understand the GISAXS peak patterns and extract quantitative information, those peaks are divided into two sets of scattering events (TT and RT): In the TT event, the transmitted X-ray is directly scattered and then transmitted through the sample; therefore, no reflection is involved. On the other hand, RT represents the event that the X-ray reflected from the substrate is scattered and then transmitted through the sample. In the range of the incident angles in this paper, TT and RT dominate the total scattering intensity; therefore, we consider only TT and RT in the four events in distorted wave Born approximation (DWBA).[13] While TT event has no dependence on the incident angle, RT has dependence on the incident angle because reflection is involved. For example, the direct beam position of RT is $q_z = (4\pi/\lambda)\sin\alpha$, while that of TT is $q_z = 0$; therefore, the scattered X-ray appears relative to those two scattering centers. To confirm the hypothesis and to

distinguish between those two sets of peaks, two different incident angles α were chosen and the scattering patterns were compared in Figure 5a and their intensities along z-axis are plotted in Figure 5b. The stationary peaks are assigned to TT and the shifting peaks with increasing α are assigned to RT since only the scattering center of RT moves with α. One can find that each set of peaks is evenly spaced, which clearly indicates the existence of parallel stacking nanosheets over the entire substrate. The assignment of peaks is found in Figure 5b as 1, 2, and 3 and 1′, 2′, and 3′. The spacing of nanosheets was consistently obtained to be 20.9 ± 0.4 nm from $2\pi/\Delta q_z$ of two sets of peaks at two incident angles, where Δq_z is the difference between the adjacent peaks in the same set.

It should be noted that this structure is not a simple densely packed lamellar structure but separated bcp bilayer sheets, which can be justified with the following reasons: (1) the GISAXS intensity of nanosheets is more than an order of magnitude stronger than that of the as-cast films before the process. (The exposure times to avoid saturation of the X-ray detector are $100\sim500$ ms and $5\sim10$ s for the processed and the unprocessed films, respectively.) Therefore, the electron density contrast increased with the voids introduced by the process. (2) SEM clearly shows the layered structures despite the fact that SEM is not capable of distinguishing between PS and PFMA domains due to their poor electronic contrast. Upon depressurization, the swollen lamellae would have collapsed to dense lamellae if the swollen lamellae were defect-free. However, the existence of defects bridging lamellae prevents the lamellae from collapsing completely. Evidently, such defects supporting the nanosheets are occasionally found in Figure 4a. Because the preferential segregation of PFMA domains to the surface is even more enhanced in CO_2[21] than that in air or in a vacuum, the CO_2 interface induces parallel orientation of swollen lamellae. Therefore, after freezing and depressurization, parallel orientation of stacking nanosheets is preferentially formed.

As already mentioned, casting from HFB induces the poorly but perpendicularly oriented PS cylinders to the surface in the PFMA matrix. Such films were processed with CO_2 in the same manner. Surprisingly, we found perpendicularly standing nanosheets on substrates. An example of SEM images has been shown in Figure 4b and its GISAXS pattern in Figure 6a. The GISAXS pattern in Figure 6a confirms that such vertically standing nanosheet structure is not just a local structure but extends over the entire film. We plotted in Figure 6b the GISAXS intensities as a function of q_y at the q_z of the maximum-intensity for the incident angles of 0.10, 0.15, and 0.20. The higher order peaks appear roughly at integer multiples of the first order peak position, which is a characteristic of a one-dimensionally alternating structure with sharp interfaces.

With careful inspection, the first order peak is actually composed of two peaks at q_{y1} (0.28 nm^{-1}) and q_{y2} (0.31 nm^{-1}), which correspond to the characteristic lengths of 22.4 and 20.3 nm, respectively. It should also be noted that q_{y2} dominates the peak for an incident angle of 0.10 (less than the critical angle of the film), while q_{y1} becomes stronger as the incident angle increases. Such a trend indicates that the distribution of nanosheet spacing is bimodal and the space between the nanosheets is smaller near the surface but is wider near the substrate. Presumably, as CO_2 evaporate, the vertical sheets start to collapse, but the bottoms of the sheets are fixed onto the substrate, which prevents the sheets from collapsing. An SEM image of the film surface and a schematic picture of the vertical standing nanosheets with the probable chain conformation are shown in Figure 7a,b, respectively. Many crevasses appear as a result of collapse of the top part of the vertical sheets. A possible cause of collapse can be capillary condensation of liquid CO_2. Although such capillary condensation might be avoided
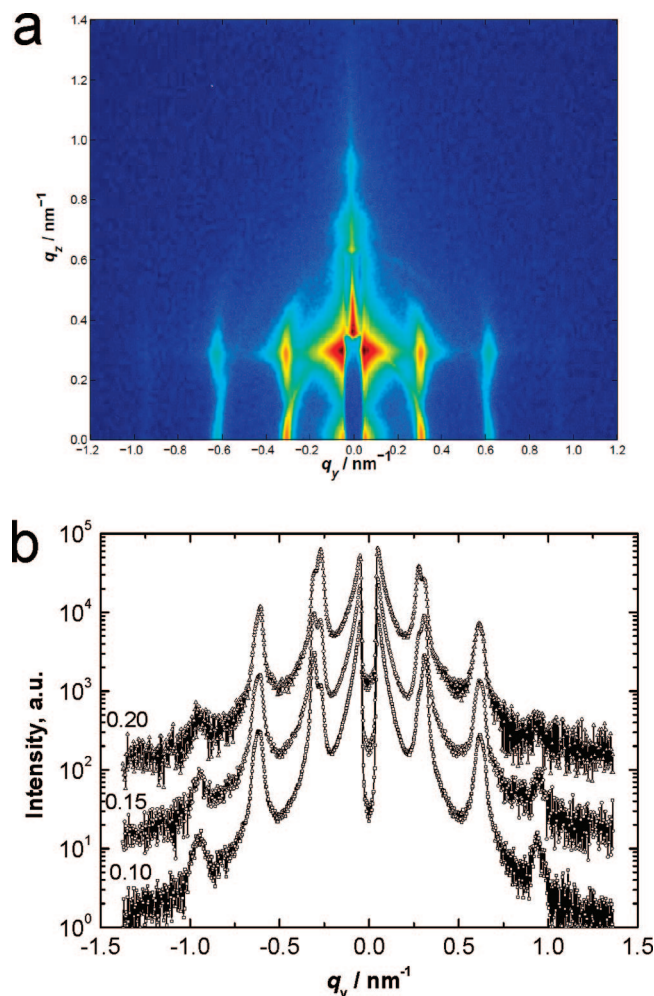
Figure 6. (a) Grazing incident small-angle X-ray scattering (GISAXS) patterns of the nanosheet films. q_y and q_z are the wave vectors parallel and perpendicular to the film plane, respectively. On the z-axis, a rectangular beam-stopper and attenuator are installed. (b) The GISAXS intensities of the vertically standing nanosheets on a substrate are plotted as a function of the in-plane component of the wave vector, q_y, for three different incident angles (0.10, 0.15, and 0.20), respective to the surface plane. The off-plane component q_z of the maximum intensity was selected.

by venting from supercritical state, venting at 35 °C or above destroyed the porous structure apparently because PS skeleton domains is too soft to support the porous structure during depressurization since T_g of PS is approximately 30 °C in CO_2.

As already discussed, the segregation of PFMA should induce the parallel orientation of the nanosheets; however, the vertical orientation of the PS cylinders in the as-cast state tend to form the bilayer nanosheets parallel to the cylinder axis and therefore perpendicular to the surface since the cylinders perpendicular to the surface are easily merged into the lamellae vertical to the surface. Although this structure may change to the parallel orientation, which is the probable equilibrium structure, we did not observe such a morphological change in our experimental condition.

The horizontally and vertically aligned nanosheet structures have almost the same spacings, but the vertical nanosheets near the substrate have slightly larger spacing due to the presence of substrate, which prevents the lamellae from collapsing upon depressurization. The appearance of nanosheet structures after the process is equivalent to the lamellar morphology in CO_2, which is different from either the as-cast morphology or that expected from the block fraction. It is reasonable to conclude
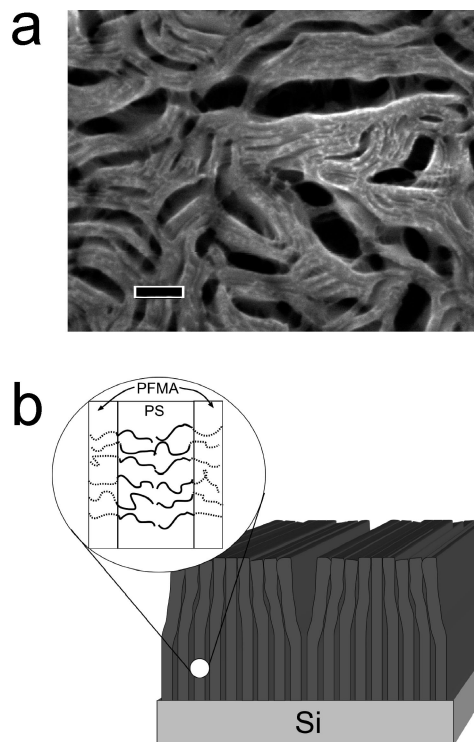

Figure 7. (a) The SEM top view of the same nanosheet film shows many crevasses appear on the film surface. The bar indicates 200 nm. (b) A schematic picture of vertically standing nanosheets with a picture of the probable chain conformation in the sheet.

that the selective swelling of the minority PFMA domains with CO_2 increases the effective volume fraction of PFMA domains and induces morphological transition to lamellae.

Conclusion

Selective swelling of PS-PFMA thin films with CO_2 induces morphological changes to swollen lamellar morphology during the CO_2 process, and horizontally and vertically stacking nanosheet structures appear after the CO_2 process. The orientations of the swollen lamellae during the process and stacking nanosheets after the process are dependent on the anisotropy of the initial morphologies for which the selectivity of casting solvent plays an important role.

Supporting Information Available: A high-resolution version of Figure 1c and DSC results. This material is available free of charge via the Internet at http://pubs.acs.org.

References and Notes

(1) Hamley, I. W. *Angew. Chem., Int. Ed.* **2003**, *42*, 1692–1712.
(2) Park, C.; Yoon, J.; Thomas, E. L. *Polymer* **2003**, *44*, 6725–6760.
(3) Hillmyer, M. A. *Adv. Polym. Sci.* **2005**, *190*, 137–181.
(4) Lee, J.-S.; Hirao, A.; Nakahama, S. *Macromolecules* **1988**, *21*, 274–276.
(5) Zalusky, A. S.; Olayo-Valles, R.; Taylor, C. J.; Hillmyer, M. A. *J. Am. Chem. Soc.* **2001**, *123*, 1519–1520.
(6) Thurn-Albrecht, T.; Steiner, R.; DeRouchey, J.; Stafford, C. M.; Huang, E.; Bai, M.; Tuominen, M.; Hawker, C. J.; Russell, T. P. *Adv. Mater.* **2000**, *12*, 787–791.

(7) Yokoyama, H.; Li, L.; Nemoto, T.; Sugiyama, K. *Adv. Mater.* **2004**, *16*, 1542–1546.

(8) Yokoyama, H.; Sugiyama, K. *Macromolecules* **2005**, *38*, 10516–10522.

(9) Li, L.; Yokoyama, H.; Nemoto, T.; Sugiyama, K. *Adv. Mater.* **2004**, *16*, 1226–1229.

(10) Li, L.; Nemoto, T.; Sugiyama, K.; Yokoyama, H. *Macromolecules* **2006**, *39*, 4746–4755.

(11) Li, L.; Yokoyama, H. *Angew. Chem., Int. Ed.* **2006**, *45*, 6338–6341.

(12) Sugiyama, K.; Nemoto, T.; Koide, G.; Hirao, A. *Macromol. Symp.* **2002**, *181*, 135–153.

(13) Yokoyama, H.; Dutriez, C.; Li, L.; Nemoto, T.; Sugiyama, K.; Sasaki, S.; Masunaga, H.; Takata, M.; Okuda, H. *J. Chem. Phys.* **2007**, *127*, 014904−19.

(14) (a) Hillmyer, M. A.; Lodge, T. P. *J. Polym. Sci., Part A: Polym. Chem.* **2002**, *40*, 1–8. (b) Ren, Y.; Lodge, T. P.; Hillmyer, M. A. *Macromolecules* **2002**, *35*, 3889–3894.

(15) Yokoyama, H. *Mater. Sci. Eng. R* **2006**, *53*, 199–248.

(16) Kim, G.; Libera, M. *Macromolecules* **1998**, *31*, 2569–2577. (b) Kim, S. H.; Misner, M. J.; Russell, T. P. *Adv. Mater.* **2004**, *16*, 2119–2123. (c) Sidorenko, A.; Tokarev, I.; Minko, S.; Stamm, M. J. *J. Am. Chem. Soc.* **2003**, *125*, 12211–12216. (d) Park, S.; Wang, J.-Y.; Kim, B.; Chen, W.; Russell, T. P. *Macromolecules* **2007**, *40*, 9059–9063.

(17) Yokoyama, H.; Tanaka, K.; Takahara, A.; Kajiyama, T.; Sugiyama, K.; Hirao, A. *Macromolecules* **2004**, *37*, 939–945.

(18) A high resolution image is available in Supporting Information.

(19) Condo, P. D.; Paul, D. R.; Johnston, K. P. *Macromolecules* **1994**, *27*, 365–371.

(20) Wang, W.-C. V.; Kramer, E. J.; Sachse, W. H. *J. Polym. Sci., Part B: Polym. Phys.* **1982**, *20*, 1371–1384.

(21) Yokoyama, H.; Sugiyama, K. *Langmuir* **2004**, *20*, 10001–10006.